DISTRIBUTED SINGLE-REED MODELING BASED ON ENERGY QUADRATIZATION AND APPROXIMATE MODAL EXPANSION

Champ C. Darabundit *
CIRMMT
McGill University
Montréal, Canada
champ.darabundit@mail.mcgill.ca

Vasileios Chatziioannou
University of Music and Performing Arts
Vienna
Vienna, Austria
chatziioannou@mdw.ac.at

Gary Scavone
CIRMMT
McGill University
Montréal, Canada
gary.scavone@mcgill.ca

ABSTRACT

Recently, energy quadratization and modal expansion have become popular methods for developing efficient physics-based sound synthesis algorithms. These methods have been primarily used to derive explicit schemes modeling the collision between a string and a fixed barrier. In this paper, these techniques are applied to a similar problem: modeling a distributed mouthpiece lay-reed-lip interaction in a woodwind instrument. The proposed model aims to provide a more accurate representation of how a musician's embouchure affects the reed's dynamics. The mouthpiece and lip are modeled as distributed static and dynamic viscoelastic barriers, respectively. The reed is modeled using an approximate modal expansion derived via the Rayleigh-Ritz method. The reed system is then acoustically coupled to a measured input impedance response of a saxophone. Numerical experiments are presented.

1. INTRODUCTION

A fundamental phenomenon in the excitation of single-reed instruments — such as the clarinet and saxophone — involves the reed interacting with, or beating against, the lay of the mouthpiece [1]. Reed beating not only restricts the flow of air into the instrument but also introduces nonlinear collision effects to the flow. Historically, the single reed has been modeled in a lumped manner with a mass-spring-damper system representing the displacement of the reed tip [2, 3]. More recently, collision effects have been included in the lumped model using the nonlinear viscoelastic Hunt-Crossley (HC) contact model [4].

An issue with the lumped approach is the entanglement of player and material parameters. The lumped parameters must encapsulate the effects of the player's embouchure and the material properties of the reed. Likewise, the lumped collision must compensate for the complex distributed interaction between the reed and the curved mouthpiece lay. This has motivated more intensive treatments that model the reed as a cantilever Euler-Bernoulli beam [5]. However, collision with the lay and interaction with the player's lip have only been approached in an ad-hoc manner.

This article proposes a refinement to the distributed single-reed model by modeling contact with the lay and the player's lip using distributed HC-type forces. While the lip is not colliding with the reed, per se, the biomechanical behavior of tissue exhibits nonlinear dissipation and spring hardening [6, Ch. 7], motivating the application of the HC model here. The intent behind modeling the lip as a separate and dynamic object is to have playing parameters that directly represent a wind musician's embouchure.

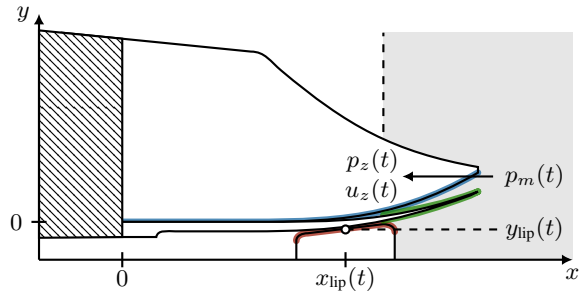

Figure 1: Lay-reed-lip system omitting the upper lip and teeth. The reed is clamped below the ligature (hatched). The lay ($\mathcal{A}$) and lip ($\mathcal{B}$) domains are marked blue and red, respectively. The acoustic domain ($\mathcal{P}$, green) is applied to the reed surface in the region above the lip (shaded gray).

The proposed model is efficiently simulated using recent algorithmic advances in collision modeling based on the scalar auxiliary variable (SAV) approach [7, 8, 9]. Prior results on distributed collisions are extended by transforming elastic interactions into viscoelastic interactions. Additionally, a novel approach is taken to modeling the lip as a moving distributed barrier. The energy-based Rayleigh-Ritz method [10] is used to derive an approximate modal expansion of the reed based on its spatially varying cross-sectional area. The Rayleigh-Ritz method has been used in musical acoustics to derive the modal parameters of plates [11]. Because the reed operates at playing frequencies below its own resonant frequency, only a few modes are necessary to capture the reed dynamics. The excitation mechanism is coupled to a lumped modal instrument impedance response derived from measurement of an alto saxophone.

Sec. 2 introduces the governing equations of the lay-reed-lip system, the acoustic flow, and the modal bore. In Sec. 3, the reed's modes are derived using the Rayleigh-Ritz method and demonstrated to converge with a high resolution finite difference scheme. Sec. 4 discretizes the system using finite-difference time-domain (FDTD) methods and outlines the update of the numerical scheme. Sec. 5 describes the optimization procedure used to obtain a modal instrument response from saxophone impedance measurements. Sec. 6 presents the results of numerical simulation experiments. Sec. 7 provides concluding remarks and ideas for future work.

* This work was supported by the Natural Sciences and Engineering Research Council of Canada (NSERC) through the Vanier Canada Graduate Scholarships program.

2. GOVERNING EQUATIONS

In this article, d_z^n and ∂_z^n are used to denote the n$^{\text{th}}$ total and partial derivatives with respect to a general variable z. Let $\bar{y}(x,t)$ represent the transverse displacement of the reed, of length L, defined on the domain $\mathcal{L} = [0, L]$. The lay-reed-lip system, displayed in Fig. 1, is governed by the following equation:

$$\rho_r S(x) \left(\partial_t^2 \bar{y} + \gamma \partial_t \bar{y}\right) + \partial_x^2 \left(EI(x)(1 + \eta \partial_t)\partial_x^2 \bar{y}\right) = \mathcal{F}, \quad (1)$$

where ρ_r is the material density of the reed, E is Young's modulus of elasticity, γ is a damping constant related to the viscosity of air, and η is another damping constant related to internal damping in the reed. $S(x)$ and $I(x)$ are the spatially varying cross-sectional area and area moment of inertia, respectively. The reed is modeled as a rectangular cantilever Euler-Bernoulli beam and is parameterized by a thickness function $b(x)$ such that

$$S(x) = wb(x), \quad I(x) = \frac{S(x)b^2(x)}{12}, \quad (2)$$

where w is the width of the reed. Following [5], the thickness is defined relative to the top of the reed. The reed is subject to the following clamped-free boundary conditions:

$$\bar{y}(0,t) = \partial_x \bar{y}(0,t) = 0, \; \partial_x^2 \bar{y}(L,t) = \partial_x EI(L) \partial_x^2 \bar{y}(L,t) = 0. \quad (3)$$

The term $\mathcal{F} = \mathcal{F}(x,t)$ is the force per unit length applied to the reed which can be decomposed into contributions from the lay, lip, and instrument

$$\mathcal{F} = \mathcal{F}_b - \mathcal{F}_a + \mathcal{F}_p. \quad (4)$$

$\mathcal{F}_a$ and $\mathcal{F}_b$ are the contact densities due to the barriers above (lay) and below (lip) the reed, respectively. $\mathcal{F}_p$ is the acoustic force density resulting from the pressure difference upstream and downstream of the reed. Each force density is defined over its own domain ($\mathcal{A}$, $\mathcal{B}$, $\mathcal{P}$) inside $\mathcal{L}$, and these domains can and do overlap.

2.1. Lay and lip models

The contact densities $\mathcal{F}_a$ and $\mathcal{F}_b$ are modeled as distributed nonlinear viscoelastic contact forces based on the Hunt-Crossley (HC) model [12]. This approach has been used to model lumped reed collisions in [13]. A general distributed contact density, $\mathcal{F}_c$, over a domain $\mathcal{C} = [x_{c,1}, x_{c,2}]$ is defined as

$$\mathcal{F}_c = (1 + c(x)\partial_t h)\, \partial_h \mathcal{V}_c(h), \quad (5)$$

and is dependent on the compression $h = h(x,t)$. $c(x)$ is the non-negative possibly distributed contact damping and

$$\mathcal{V}_c(h) = \frac{k(x)}{\alpha(x)+1} \left[h\right]_+^{\alpha(x)+1}, \quad \left[\cdot\right]_+ = \max(\cdot, 0), \quad (6)$$

defines the contact potential density. $k(x)$ is the non-negative possibly distributed contact stiffness and $\alpha(x)$ is a geometric exponent. The contact damping is defined to be constant during contact, but dependent on the impact velocity such that a consistent coefficient of restitution, c_r, is achieved [14, 15]. For the force densities in (4), the respective compressions are defined as

$$h_a(x) = \bar{y} - \bar{y}_a(x), \quad (7a)$$

$$h_b(x,t) = \bar{y}_b(x,t) - (\bar{y} - b(x)), \quad (7b)$$

for the barriers above and below the reed located at $\bar{y}_a(x)$ and $\bar{y}_b(x)$, respectively. The total contact potential is

$$V_c = \int_{\mathcal{C}} \mathcal{V}_c(h) dx. \quad (8)$$

2.2. Scalar auxiliary variable method

The scalar auxiliary variable (SAV) method [16] is an energy quadratization method which has seen widespread use in developing explicit or linearly implicit schemes for nonlinear systems [17]. Through a change of variables, energy quadratization methods encode a nonlinear system into a time-varying linear system. The total contact potential energies, V_a and V_b, for the lay and lip respectively now define a scalar auxiliary variable

$$\psi = \sqrt{2(V_a + V_b) + \epsilon}, \quad (9)$$

where ϵ is a small gauge. The contact force densities are rewritten as

$$\mathcal{F}_a = \psi g_a + r_a(x,t)\partial_t h_a, \quad \mathcal{F}_b = \psi g_b + r_b(x,t)\partial_t h_b, \quad (10)$$

where g_a and g_b are the variational derivatives of ψ with respect to the compressions h_a and h_b. g_a and g_b are defined generally based on the variation derivative of ψ with respect to the compressions as

$$g_{a,b} = \frac{\delta \psi}{\delta h_{a,b}} = \frac{k_{a,b}(x)}{\sqrt{2(V_a + V_b) + \epsilon}} \left[h_{a,b}\right]_+^{\alpha_{a,b}}. \quad (11)$$

r_a and r_b are time-varying nonlinear damping coefficients equal to

$$r_{a,b} = c_{a,b}(x)\, \partial_{h_{a,b}} \mathcal{V}_c(h_{a,b}), \quad (12)$$

which are guaranteed non-negative by the non-negativity of $\partial_{h_{a,b}} \mathcal{V}_c(h_{a,b})$ and $c_{a,b}$. Unlike in the lumped case [15, 18], the damping coefficients are not expressed in terms of the gradient and auxiliary variables. The time-derivative of the auxiliary variable follows

$$d_t \psi = \int_{\mathcal{A}} g_a \partial_t h_a dx + \int_{\mathcal{B}} g_b \partial_t h_b dx. \quad (13)$$

2.3. Acoustic forces and flow

The acoustic force density is defined over the domain $\mathcal{P}$

$$\mathcal{F}_p = w\, p_\Delta(t), \quad p_\Delta = p_m(t) - p_z(t), \quad (14)$$

where p_m is the upstream pressure in the player's mouth and p_z is the downstream pressure in the instrument. Owing to the lumped model of the bore impedance, the total flow entering the bore, u_z, is modeled in an ad hoc manner based on a simple and quasi-stationary Bernoulli flow [1]

$$u_z = u_f + \int_{\mathcal{P}} \mathcal{U}_r dx, \quad \mathcal{U}_r = w \partial_t \bar{y}, \quad (15)$$

with

$$u_f = \text{sign}(p_\Delta)\, S_j \sqrt{2\left|p_\Delta\right|/\rho_a}, \quad (16)$$

and S_j the jet aperture area and ρ_a the density of air. S_j will be defined later on in Sec. 4.4. $\mathcal{U}_r$ is a volume flow density representing the reed pumping flow.

2.4. Modal instrument impedance

The instrument bore is modeled via a modal system representing the modal expansion of the instrument's input acoustic impedance. This approach is common in modal synthesis and was also used

to model wind instruments based on impedance measurements in [19]. The result is a set of M ordinary differential equations,

$$u_z \mathbf{1}_M = \mathbf{M}_z d_t \mathbf{p} + 2\mathbf{R}_z \mathbf{p} + \mathbf{K}_z \mathbf{q}, \tag{17a}$$

$$d_t \mathbf{q} = \mathbf{p}, \qquad p_z = \mathbf{1}_M^T \mathbf{p}. \tag{17b}$$

$\mathbf{q}$ and $\mathbf{p}$ both $\in \mathbb{R}^{M\times 1}$ are the acoustic momentum per unit area and pressure of each mode, respectively. $\mathbf{1}_M$ is an M column vector of ones. The diagonal parameter matrices $\mathbf{M}_z$, $\mathbf{R}_z$, and $\mathbf{K}_z$ are the modal mass, damping, and stiffness matrices with diagonal elements defined by

$$M_{mm} = m_m,\ R_{mm} = m_m \zeta_m \omega_m,\ K_{mm} = m_m \omega_m^2, \tag{18}$$

with m_m the acoustic mass, ζ_m the damping ratio, and ω_m the resonant frequency in rads/s of each mode.

2.5. Energy balance

The system in (1) obeys the following energy balance

$$d_t \underbrace{(H_r + V_c + H_z)}_{H} = \underbrace{P_b + P_m}_{P} - \underbrace{(Q_r + Q_c + Q_f + Q_z)}_{Q}, \tag{19}$$

where H is the total stored energy of the system, Q is the total power loss, and P is the total supplied power. Each total energetic element has been broken down into its constituent subsystems with the contact related quantities defined as $V_c = V_a + V_b$ and $Q_c = Q_a + Q_b$. The energy balance is derived by taking the product of $\partial_t \bar{y}$ and (1), integrating over the entire domain, and using the definitions in (5)-(17b)

$$H_r = \frac{1}{2}\int_{\mathcal{L}} \rho_r S \left(\partial_t y\right)^2 dx + EI\left(\partial_x^2 y\right)^2 dx, \tag{20a}$$

$$V_c = \int_{\mathcal{A}} \mathcal{V}_a(h_a) dx + \int_{\mathcal{B}} \mathcal{V}_b(h_b) dx = \frac{1}{2}\psi^2, \tag{20b}$$

$$H_z = \frac{1}{2}\left\|\sqrt{\mathbf{M}_z}\mathbf{p}\right\|^2 + \frac{1}{2}\left\|\sqrt{\mathbf{K}_z}\mathbf{q}\right\|^2, \tag{20c}$$

$$Q_r = \int_{\mathcal{L}} \gamma \rho_r S \left(\partial_t y\right)^2 + \eta EI\left(\partial_t \partial_x^2 y\right)^2 dx, \tag{20d}$$

$$Q_c = \int_{\mathcal{A}} r_a(x,t)\left(\partial_t h_a\right)^2 dx + \int_{\mathcal{B}} r_b(x,t)\left(\partial_t h_b\right)^2 dx, \tag{20e}$$

$$Q_f = p_\Delta u_f = S_j \sqrt{\frac{2}{\rho_a}}\left|p_\Delta\right|^{3/2},\ Q_z = \left\|\sqrt{2\mathbf{R}_z} d_t \mathbf{q}\right\|^2, \tag{20f}$$

$$P_b = \int_{\mathcal{B}} \partial_t y_b \mathcal{F}_b dx, \quad P_m = p_m u_z, \tag{20g}$$

where vector norm and inner product are defined as

$$\langle \mathbf{u}, \mathbf{v}\rangle = \mathbf{u}^T \mathbf{v}, \quad \|\mathbf{u}\| = \sqrt{\langle \mathbf{u}, \mathbf{u}\rangle}. \tag{21}$$

If all the system parameters are non-negative then H and Q are ≥ 0 and the proposed system in (1) is passive.

3. APPROXIMATE MODAL EXPANSION

Modal expansion methods involve expressing a system as a superposition of N modal displacements,

$$\bar{y}(x,t) = \sum_{n=1}^{N} v_n(x) y_n(t), \tag{22}$$

where v_n is the corresponding spatial eigenfunction. Said methods typically rely on an analytical solution for the spatial eigenfunctions [20, 21]. However, no analytical solution exists for the cantilever beam and further complexity results from systems with distributed parameters — i.e. varying thickness — as is the case here.

The Rayleigh-Ritz method is an energy-based method which can be used to approximately solve a differential eigenvalue problem [10]. Instead of analytical eigenfunctions, approximate Ritz eigenfunctions are formed by a superposition of trial functions ϕ_n and undetermined coefficients a_n,

$$v_n^{(N_r)} = \sum_{n=1}^{N_r} a_n \phi_n(x). \tag{23}$$

N_r denotes the number of trial functions used in the approximation. The set of trial functions must be admissible functions and satisfy the boundary conditions of the system. A good choice of trial functions are the spatial eigenfunctions of a related system or ones designed to observe the boundary condition [22]. The coefficients, a_n, are found by solving the algebraic eigenvalue problem

$$\mathbf{K}\mathbf{a} = \left(\omega_n^{(N_r)}\right)^2 \mathbf{M}\mathbf{a}, \tag{24}$$

where $\omega_n^{(N_r)}$ is the n$^{\text{th}}$ Ritz eigenfrequency. $\mathbf{K}$ and $\mathbf{M}$ are the so-called symmetric stiffness and mass matrices with elements

$$k_{ij} = \int_0^L EI(x)\left(\partial_x^2 \phi_i(x)\right)\left(\partial_x^2 \phi_j(x)\right) dx, \tag{25a}$$

$$m_{ij} = \int_0^L \rho_r A(x) \phi_i(x) \phi_j(x) dx, \tag{25b}$$

which arise from minimizing the ratio of the reference potential energy and maximum kinetic energy in (20a). These elements are derived, in this paper, through a numerical integration. Interested readers are referred to [10, Ch. 9] for further details. Utilizing an approximate modal expansion in vector form $\bar{y}(x,t) = \mathbf{V}^{(N_r)}\mathbf{y}(t)$, taking the product with the transpose of $\mathbf{V}^{(N_r)}$, and integrating over the domain produces the modal form of (1)

$$d_t^2 \mathbf{y} + \underbrace{\left(\gamma \mathbf{I} + \eta \mathbf{\Omega}^2\right)}_{2\mathbf{R}} d_t \mathbf{y} + \mathbf{\Omega}^2 \mathbf{y} = \mathbf{F}, \tag{26}$$

based on the definitions in (25) and the orthogonality of the norm normalized trial functions. $\mathbf{\Omega}$ is a diagonal matrix containing the approximate Ritz eigenfrequencies, $\omega_n^{(N_r)}$, and $\mathbf{F}$ is a column vector containing the modal forces with elements

$$F_n(t) = \int_{\mathcal{L}} v_n^{(N_r)} \mathcal{F}(x,t) dx. \tag{27}$$

In practice, the number of modes used in the Rayleigh-Ritz method is greather than the number of modes used in the approximate modal expansion ($N \leq N_r$). The accuracy of the method increases with the number of trial functions, but the higher mode estimates are less accurate and likely outside the range of interest for audio applications. For the system in (1), trial functions were chosen from the set of constant parameter cantilever eigenfunctions [10, Ex. 8.4, Eq. (o)], with mode amplitudes A_r chosen such that the $\mathcal{L}_2$ norm of each trial function is unity. Special care was taken such that the boundary conditions are met numerically.

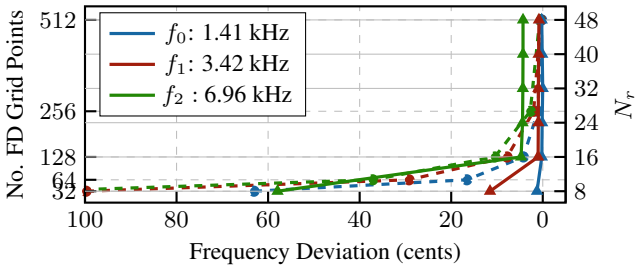

Figure 2: Convergence of the first three reed modes obtained via the Rayleigh-Ritz method (solid) and the FD θ-scheme (dashed) to the same FD scheme with 2048 spatial grid points.

Based on the modal expansion, the stored energy and dissipated power in the reed is rewritten as

$$H_r = \frac{1}{2}\left\|d_t\mathbf{y}\right\|^2 + \frac{1}{2}\left\|\mathbf{\Omega}\mathbf{y}\right\|^2, \quad Q_r = \left\|\sqrt{2\mathbf{R}}d_t\mathbf{y}\right\|^2 \tag{28}$$

Fig. 2 compares the convergence of the first three modes for the saxophone reed geometry and parameters given in [5] obtained via the Rayleigh-Ritz method and the finite difference (FD) θ-scheme used in the same article. The ground truth was considered to be the θ-scheme with 2048 grid points and sampling rate 96×10 kHz. The Rayleigh-Ritz method with $N_r \geq 16$ demonstrates nearly equivalent accuracy to the θ-scheme with 512 grid points and the same sampling rate. The third mode deviates by approximately five cents from the ground truth. This is likely due to errors in the numerical integration used to compute the modes.

4. DISCRETE SYSTEM

The system described thus far is discretized using finite difference time domain (FDTD) methods. First, discrete operators are introduced. Then, each element of the system is discretized. Finally, a method for updating the entire system is presented.

4.1. Discretization operators

Let z_l^n represent the discrete sampling of a function $z(\Delta_t n, \Delta_x l)$ where Δ_t and Δ_x are the temporal and spatial grid spacing, respectively. Defining the half temporal shift operator $e_{t\pm}z_l^n = z_l^{n\pm\frac{1}{2}}$, first-order partial and total time derivatives can be approximated by the following operators

$$\delta_t = \frac{e_+ - e_-}{\Delta_t}, \quad \delta_{t\cdot} = \frac{e_+^2 - e_-^2}{2\Delta_t}. \tag{29}$$

Unity is approximated by the following operators

$$\mu_t = \frac{e_+ + e_-}{2}, \quad \mu_{t\cdot} = \frac{e_+^2 + e_-^2}{2}, \tag{30}$$

and higher order temporal derivatives and approximations of unity can be produced by combining the operators above. Approximations used in this article are

$$\delta_{tt} = \frac{e_+^2 - 2 + e_-^2}{\Delta_t^2} \approx \partial_t^2, \quad \mu_{tt} = \frac{e_+^2 + 2 + e_-^2}{4} \approx 1. \tag{31}$$

Although spatial derivatives have been eliminated by the modal expansion approach, spatial integrals need to be approximated via Riemann sums

$$\Delta_x \sum_{l=1}^{N} u_l \approx \int_{\mathcal{L}} u dx. \tag{32}$$

Significantly, variables and forces defined on different domains are related to the modal displacements via projection matrices. Consider, generally, a set of N_d observation points $\mathbf{x}_d$ with spatial sampling Δ_x^d. The projection matrix mapping the observation points to the modal displacement is defined based on the spatial eigenfunctions as

$$\mathbf{P}_d = \left[v_1^{(N_r)}(\mathbf{x}_d), \ldots, v_N^{(N_r)}(\mathbf{x}_d)\right]^T \in \mathbb{R}^{N\times N_d}. \tag{33}$$

Defining the discrete displacements $\hat{\mathbf{y}}_d$ and force densities $\hat{\mathbf{f}}_d$, the discrete form of the modal expansion (22) and modal force (27) are

$$\hat{\mathbf{y}}_d = \mathbf{P}_d^T\mathbf{y}_d, \quad \mathbf{F}_d = \Delta_x^d\mathbf{P}_d\hat{\mathbf{f}}_d, \tag{34}$$

and d can be replaced with a, b, or p.

4.2. Modal reed discretization

The modal expansion of the reed (26) is discretized as

$$\delta_{tt}\mathbf{y}^n + 2\mathbf{R}\delta_{t\cdot}\mathbf{y}^n + \mathbf{\Omega}^2\mu_{tt}\mathbf{y}^n = \mathbf{F}^n, \tag{35}$$

where $\mathbf{y}$ and $\mathbf{F} \in \mathbb{R}^{N\times 1}$ are the discrete modal displacement and force vectors. The modal forces are defined as

$$\mathbf{F}^n = \Delta_x^b\mathbf{f}_b^n - \Delta_x^a\mathbf{f}_a^n + \Delta_x^p\mathbf{f}_p^n. \tag{36}$$

$\mathbf{f}_b^n$, $\mathbf{f}_a^n$, and $\mathbf{f}_p^n$ are the projected force densities from the lay, lip, and instrument acoustics.

The modal parameters in (26) are pre-warped to account for numerical dispersion in the scheme following [20]. Solving (35) for $\mathbf{y}^{n+1}$ results in the update scheme

$$\mathbf{y}^{n+1} = \mathbf{A}\mathbf{y}^n + \mathbf{B}\mathbf{y}^{n-1} + \mathbf{C}\mathbf{f}, \tag{37}$$

where $\mathbf{A}$, $\mathbf{B}$, and $\mathbf{C}$ are diagonal matrices $\in \mathbb{R}^{N\times N}$.

4.3. Lay and lip discretization

The lay and lip are defined on two subspaces based on the compression vectors above the reed, $\acute{\mathbf{h}}_a^n \in \mathbb{R}^{N_a\times 1}$, and below the reed, $\breve{\mathbf{h}}_b^n \in \mathbb{R}^{N_b\times 1}$. The *acute* $\acute{[\cdot]}$ and *breve* $\breve{[\cdot]}$ markers are used to demarcate elements defined in their respective subspaces. The discrete time-derivates of the compressions are related to the modal displacements by

$$\delta_{t\cdot}\acute{\mathbf{h}}_a^n = \mathbf{P}_a^T\delta_{t\cdot}\mathbf{y}^n, \quad \delta_t\breve{\mathbf{h}}_b^n = \delta_t\breve{\mathbf{y}}_b^n - \mathbf{P}_b^T\delta_{t\cdot}\mathbf{y}^n. \tag{38}$$

The lip barrier utilizes the interleaved centered difference, δ_t, to allow for player inputs before the $n+1$ timestep. Using the relationship in (38), the projected modal contact force densities containing the discrete form of (10) are written in terms of the modal displacements as

$$\mathbf{f}_a^n = \underbrace{\mathbf{P}_a\acute{\mathbf{g}}_a^n}_{\mathbf{g}_a^n}\mu_t\psi^n + \underbrace{\mathbf{P}_a\acute{\mathbf{R}}_a^n\mathbf{P}_a^T}_{\mathbf{R}_a^n}\delta_t\mathbf{y}^n, \tag{39}$$

$$\mathbf{f}_b^n = \underbrace{\mathbf{P}_b\breve{\mathbf{g}}_b^n}_{\mathbf{g}_b^n}\mu_t\psi^n - \underbrace{\mathbf{P}_b\breve{\mathbf{R}}_b^n\mathbf{P}_b^T}_{\mathbf{R}_b^n}\delta_t\mathbf{y}^n + \underbrace{\mathbf{P}_b\breve{\mathbf{R}}_b^n\delta_t\breve{\mathbf{y}}_b^n}_{\mathbf{r}_b^n}, \tag{40}$$

where $\acute{\mathbf{g}}_a$ and $\breve{\mathbf{g}}_b$ are the discrete form of the gradient functions, the value of which requires careful consideration and will be discussed later on in Sec. 4.8. $\acute{\mathbf{R}}_a^n$ and $\breve{\mathbf{R}}_b^n$ are time-varying diagonal damping matrices $\in \mathbb{R}^{N_a \times N_a}$ and $\mathbb{R}^{N_b \times N_b}$, respectively, with elements corresponding to the discrete-time version of (12). Based on the projection matrices and the relationships in (38), the discrete form of (13) is

$$\delta_t \psi^n = -\left(\mathbf{g}_\star^n\right)^T \delta_{t\cdot} \mathbf{y}^n + \Delta_x \left(\breve{\mathbf{g}}_b^n\right)^T \delta_t \breve{\mathbf{y}}_b^n, \tag{41}$$

with $\mathbf{g}_\star^n = \Delta_x^b \mathbf{g}_b^n - \Delta_x^a \mathbf{g}_a^n$. The capped definitions for contact stiffnesses and damping from [15] are utilized to limit numerical errors for high stiffness and restitution coefficients.

4.4. Acoustic forces and flow discretization

The acoustic interaction between the reed and acoustic flow is defined on another subspace $\hat{\mathbf{y}} \in \mathbb{R}^{N_p \times 1}$ with corresponding projection matrix $\mathbf{P}_p$. The acoustic force is only applied to the reed at positions above the lip. The force density vector is

$$\mathbf{f}_p^n = \mathbf{P}_p \hat{\mathbf{f}}_p^n = w p_\Delta^n \underbrace{\mathbf{P}_p \hat{\mathbf{1}}_p}_{\mathbf{1}_p}, \quad p_\Delta^n = p_m^n - p_z^n, \tag{42}$$

with $\hat{\mathbf{1}}_p$ an N_p column vector of ones. The discrete volume velocity flow into the instrument is

$$u_z^n = \text{sign}(p_\Delta^n) S_j^n \sqrt{2\left|p_\Delta^n\right|/\rho_a} + w \Delta_x^p \mathbf{1}_p^T \delta_{t\cdot} \mathbf{y}^n, \tag{43}$$

and the jet apeture area was arbitrary chosen based on combination of the side and tip openings

$$\begin{aligned} S_j^n &= 0.6 S_{\text{tip}}^n + 0.2\left(2 S_{\text{side}}^n\right), \\ &= 0.6w\left[-\acute{h}_{a,L}^n\right]_+ + 0.2\left(2\sum_{l \geq l_{\text{lip}}}^{L} \Delta_x^a \left[-\acute{h}_{a,l}^n\right]_+\right), \end{aligned} \tag{44}$$

with scaling constants representing a vena contracta factor.

4.5. Modal impedance discretization

The following scheme is used to discretize the modal instrument impedance,

$$u_z^n \mathbf{1}_M = \mathbf{M}_z \delta_t \mathbf{p}^n + 2\mathbf{R}_z \mu_t \mathbf{p}^n + \mathbf{K}_z \mu_t \mathbf{q}^n, \tag{45a}$$

$$\delta_t \mathbf{q}^n = \mu_t \mathbf{p}^n, \qquad p_z^n = \mathbf{1}_M^T \mu_t \mathbf{p}^n. \tag{45b}$$

The frequency response of the scheme is the same as the scheme used to discretize the reed and can be pre-warped in an identical manner.

4.6. Discrete energy analysis

The discrete energy follows from the inner product with $\delta_{t\cdot}\mathbf{y}^n$ with (35) and the relationships in Sec. 4.2-4.5. The discrete power-balance is

$$\delta_t \mathfrak{h}^n = \mathfrak{p}^n - \mathfrak{q}^n, \tag{46}$$

with $\mathfrak{h}$, $\mathfrak{p}$ and $\mathfrak{q}$ the discrete total stored energy, supplied power, and dissipated power containing discrete correlates to the quantities in (20) and (28). The scheme is unconditionally stable if all parameters are non-negative.

4.7. Scheme update

The discrete scheme detailed thus far is linearly implicit and requires a matrix inverse at each time step due to the time-varying damping matrices in (39) and (40). This is unlike the case of simple elastic collisions where an explicit algorithm is achievable [17]. Owing to the approximate modal expansion and the reed system at hand, only a 3×3 matrix inverse is required. It will be helpful, as in [8] to define an intermediate variable $\mathbf{s}^n = \mathbf{y}^{n+1} - \mathbf{y}^{n-1}$. Thus, (37) is rewritten as

$$\mathbf{s}^n = \mathbf{s}_\star^n + \mathbf{C}\mathbf{f}^n, \tag{47}$$

with $\mathbf{s}_\star^n = \mathbf{A}\mathbf{y}^n + (\mathbf{B} - \mathbf{I})\,\mathbf{y}^{n-1}$ representing the solution to $\mathbf{s}^n$ in the absence of external forces. $\mathbf{I}$ is an appropriately sized identity matrix. Rewriting (39) and (40) in terms of $\mathbf{s}^n$ and using (41), the following linear system in $\mathbf{s}^n$ is derived:

$$\underbrace{\left[\mathbf{D} + \frac{1}{4}\mathbf{g}_\star^n \left(\mathbf{g}_\star^n\right)^T\right]}_{\mathbf{E}} \mathbf{s}^n = \mathbf{C}^{-1}\mathbf{s}_\star^n + \mathbf{c}_\star^n + \Delta_x^p \mathbf{f}_p^n, \tag{48}$$

with,

$$\mathbf{D} = \mathbf{C}^{-1} + \frac{1}{2\Delta}\left(\Delta_x^a \mathbf{R}_a + \Delta_x^b \mathbf{R}_b\right), \tag{49a}$$

$$\mathbf{c}^\star = \mathbf{g}_\star^n \psi^{n-\frac{1}{2}} + \Delta_x^b \left(\frac{\Delta_t}{2}\mathbf{g}_\star^n \left(\breve{\mathbf{g}}_b^n\right)^T \delta_t \breve{\mathbf{y}}_b^n + \mathbf{r}_b^n\right), \tag{49b}$$

The inverse of $\mathbf{E}$ can be updated with the Sherman-Morrison formula as in [17],

$$\mathbf{E}^{-1} = \mathbf{D}^{-1} - \frac{\frac{1}{4}\mathbf{D}^{-1}\mathbf{g}_\star^n \left(\mathbf{g}_\star^n\right)\mathbf{D}^{-1}}{1 + \frac{1}{4}\left(\mathbf{g}_\star^n\right)^T \mathbf{D}^{-1}\mathbf{g}_\star^n}. \tag{50}$$

It is only necessary to compute the dense inverse $\mathbf{D}^{-1}$ at each time step.

The nonlinear coupling between the reed and the bore requires reformulating (45a) in terms of the discrete pressure difference, then substituting in $\mathbf{s}^n$ from (48) into (43) and solving the following quadratic in $\sqrt{|p_\Delta^n|}$

$$-c_2 p_\Delta^n - c_1^n \text{sign}\left(p_\Delta^n\right)\sqrt{\left|p_\Delta^n\right|} + c_0^n = 0, \tag{51}$$

with coefficients

$$c_2 = 1 + b_2 a_2, \quad c_1^n = b_2 S_j^n \sqrt{2/\rho_a}, \tag{52a}$$

$$c_0^n = p_m^n - b_2 a_0^n + b_0^n. \tag{52b}$$

The coefficients a_2 and a_0^n arise from the reed scheme,

$$a_2 = \frac{\left(w\Delta_x^p\right)^2}{2\Delta_t}\mathbf{1}_p^T \mathbf{E}^{-1}\mathbf{C}\mathbf{1}_p, \tag{53a}$$

$$a_0^n = \frac{w\Delta_x^p}{2\Delta_t}\mathbf{1}_p^T \mathbf{E}^{-1}\left(\mathbf{C}^{-1}\mathbf{s}_\star^n + \mathbf{c}^\star\right), \tag{53b}$$

and the b_2 and b_0^n coefficient surface from the modal impedance scheme,

$$b_2 = \mathbf{1}_M^T \mathbf{B}_z^{-1} \mathbf{1}_M^T, \quad \mathbf{B}_z = \frac{2}{\Delta_t}\mathbf{M}_z + 2\mathbf{R}_z + \frac{\Delta_t}{2}\mathbf{K}_z, \tag{54a}$$

$$b_0^n = \mathbf{1}_M^T \mathbf{B}_z^{-1}\left(\mathbf{K}_z \mathbf{q}^{n-\frac{1}{2}} - \frac{2}{\Delta_t}\mathbf{M}_z \mathbf{p}^{n-\frac{1}{2}}\right). \tag{54b}$$

As c_2, $c_1^n \geq 0$, a positive solution is guaranteed by [13]

$$\operatorname{sign}\left(p_\Delta^n\right) = \operatorname{sign}(c_0), \tag{55a}$$

$$\sqrt{|p_\Delta^n|} = \frac{-c_1 + \sqrt{c_1^2 + c_2\,|c_0|}}{2c_2}. \tag{55b}$$

The scheme is updated by first determining p_Δ^n via (55), and then deriving $\mathbf{s}^n$ (and by definition $\mathbf{y}^{n+1}$) by solving (48). Following this, the auxiliary variable ψ^n and modal instrument variables, $\mathbf{p}^{n+\frac{1}{2}}$ and $\mathbf{q}^{n+\frac{1}{2}}$, can be updated via (41), (45a), and the first equation in (45b).

4.8. Potential gradient values

When modelling collisions using the SAV approach it is necessary to constrain the auxiliary variable to be non-negative such that the contact force points outwards from the barrier and the auxiliary variable does not experience any long term drift [8]. In the model presented here, there are two gradient vectors and one auxiliary variable. A proposed solution is to only constrain one gradient vector and let the other remain at its nominal value. As the lip is assumed to be in nearly constant contact with the reed, the constraint is applied to the lay gradient variable which experiences more collisions.

The nominal discrete gradient vectors are

$$\mathbf{g}_a^n = g_a(\mathbf{h}_a^n), \quad \mathbf{g}_b^n = g_b\left(\mu_t \mathbf{h}_b^n\right), \tag{56}$$

with g_a and g_b the continuous gradient functions (11) on each respective barrier grid. As in [9], consider the system in the absence of external forces due to acoustics. Then, substituting in the solution to $\mathbf{s}^n$ into (41) and expanding the definition of $\mathbf{E}^{-1}$ using (50), the necessary constraint is

$$\begin{aligned}\frac{1}{4}\underbrace{\left(\mathbf{g}_\star^n\right)^T \mathbf{D}^{-1}\mathbf{g}_\star^n \psi^{n-\frac{1}{2}}}_{\sigma_2^n} + \underbrace{\frac{1}{2}\mathbf{g}_\star^T\mathbf{D}^{-1}\left(\mathbf{C}^{-1}\mathbf{s}_\star^n + \Delta_x^b \breve{\mathbf{R}}_b^n \delta_t \breve{\mathbf{y}}_b^n\right)}_{\sigma_1^n} \\ - \underbrace{\left(\psi^{n-\frac{1}{2}} + \Delta_t\Delta_x^b\left(\breve{\mathbf{g}}_b^n\right)^T\delta_t\breve{\mathbf{y}}_b^n\right)}_{\sigma_0^n} \leq 0.\end{aligned} \tag{57}$$

Following the procedure in [8], let $\mathbf{g}_\star^n \triangleq \gamma\hat{\mathbf{g}}_\star^n$ where $\hat{\mathbf{g}}_\star^n$ is the nominal value of the combined gradient vector and γ is a scalar $\in [0,1]$. The constraint in (57) becomes a scalar quadratic inequality in γ. The branched definition of $\mathbf{g}_\star^n$ is then

$$\mathbf{g}_\star^n = \begin{cases} \min\left(\gamma_+, 1\right)\hat{\mathbf{g}}_\star^n, & V_c^n > 0 \\ \gamma_0\,\hat{\mathbf{g}}_\star^{n-1}, & V_c^n = 0 \;\&\; V_c^{n-1} > 0 \\ \mathbf{0}, & V_c^n = V_c^{n-1} = 0 \end{cases}, \tag{58}$$

where γ_+ represents the positive solution to the inequality (57)

$$\gamma_+ = 2\frac{-\sigma_1^n + \sqrt{\left(\sigma_1^n\right)^2 + \sigma_2^n\sigma_0^n}}{\sigma_2^n}. \tag{59}$$

The branching conditions are determined by the total discrete contact energy at each time step. γ_0 has an equivalent definition to γ_+ except all the gradient values in the coefficients are evaluated at the previous time step. The second branch in (58) ensures that the auxiliary variable is equal to zero immediately after contact [8]. Finally, $\mathbf{g}_a^n$ is recovered based on $\mathbf{g}_\star^n$ and the nominal value of $\mathbf{g}_b^n$. The gradients values are first determined from (58), then the scheme is updated as before.

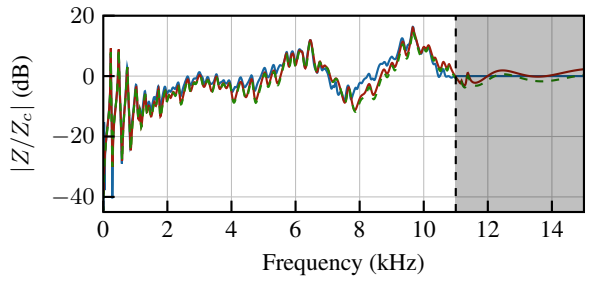

Figure 3: Normalized impedance response of a measured alto saxophone with a written G4 combined with a mouthpiece geometry (blue), optimization fit (red), and discretized response (green, dashed).

5. INSTRUMENT RESPONSE OPTIMIZATION AND MEASUREMENT

An alto saxophone without a mouthpiece was measured using a multi-microphone impedance head [23]. A CT scan of an internal mouthpiece geometry was then used to prepend a theoretical mouthpiece response to the measurement using the frequency domain transfer matrix method (TMM) [24]. The combined response was preprocessed to be minimum phase and the response above 12 kHz was set to the theoretical characteristic impedance Z_c. The response above this limit becomes progressively noisier due to the measurement range of the impedance head.

The modal parameters were estimated through a frequency banded optimization procedure akin to [25]. Instead of utilizing two separate constrained optimizations to derive the coefficients for digital filters, an unbounded Newton trust region algorithm [26] was used to fit the parameters of a continuous time model. The parameterized impedance response is

$$\hat{Z}(\theta^{(p)};\omega) = \sum_{k=1}^{K^{(p)}} \frac{e^{a_k} j\omega}{-\omega^2 - 2je^{b_k}e^{c_k}\omega + e^{2c_k}}, \tag{60}$$

where $\theta^{(p)}$ contains the set of parameters a_k, b_k, and c_k for $k = 1, \ldots, K^{(p)}$ in each optimization frequency band p. The optimization parameters are related to the modal parameters by $e^{a_k} = \frac{1}{m_k}$, $e^{b_k} = \zeta_k$, and $e^{c_k} = \omega_k$.

The parameters are optimized by minimizing the squared magnitude error between the measured impedance response, Z, within each set of P frequency bands $\omega^{(l_p)} \leq \omega \leq \omega^{(r_p)}$ using the objective function

$$\min_\theta \quad \frac{1}{2}\sum_{\omega=\omega^{(l_p)}}^{\omega^{(r_p)}} \left|Z(\omega) - \hat{Z}(\theta;\omega)\right|^2. \tag{61}$$

The log-trick parameter mapping employed here ensures all system parameters are non-negative and the optimization is unbounded. Fig. 3 compares the preprocessed alto saxophone input impedance to the frequency response of optimized modal input impedance simulated with (45a) using pre-warped parameters.

6. NUMERICAL EXPERIMENTS

Numerical experiments were conducted to evaluate the efficacy and behavior of the proposed model and algorithm. The Rayleigh-

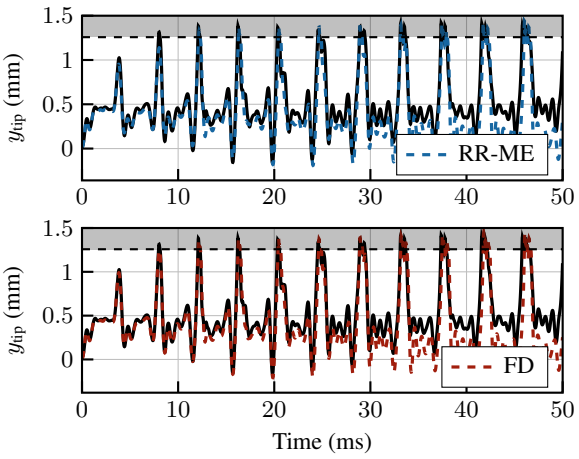

Figure 4: Comparison of approximate modal expansion (RR-ME) (blue, dashed) and the FD scheme (red, dashed) to a reference simulation with 10x oversampling at 960 kHz (black).

Ritz method was carried out using $N_r = 24$, based on the convergence demonstrated in Fig. 2. The mouthpiece lay and reed profiles were taken from [5], along with the reed material parameters. The lay parameters and lip parameters were assumed constant in each barrier. Material parameters and the lip position for the first experiment are given in Table 1 with a constant $\alpha = 1.1$ for both barriers. Sound examples can be downloaded online[1].

6.1. Embouchure warmup routine

All simulations began with an "embouchure warmup" routine, whereby the lip was moved from a non-contact state to its initial position over a duration of 1/16 seconds. During the warmup routine, the reed is uncoupled from the acoustics of the instrument to prevent any instrument resonances from being excited. This was done to reduce the length of the warmup time. Were the instrument coupled, the warmup time would need to allow for any instrument resonances to subside.

6.2. Approximate modal expansion comparison

The approximate modal expansion scheme (RR-ME) and the FD θ-scheme (FD) with 512 grid points were compared to a reference FD θ-scheme with 10x oversampling in Fig. 4. The mouth pressure, p_m, was set to a constant 2.5 kPa and actuated following the warmup routine. Both schemes closely follow the behavior of the reference scheme and display a slight drift in the response after repeated collisions. There is a noticeable difference when comparing the less elastic lip collision in the reference to the RR-ME and FD schemes. The behavior of the RR-ME scheme is comparable to the FD scheme at a much lower computational cost.

[1]https://caml.music.mcgill.ca/doku.php?id=projects:wspp

Parameter	Value	Parameter	Value
k_{lay}	1×10^8 N/m$^\alpha$	k_{lip}	6.5×10^5 N/m$^\alpha$
$c_{r,\text{lay}}$	0.8	$c_{r,\text{lip}}$	1×10^{-3}
center x_{lip}	15 mm	y_{lip}	-0.4 mm

Table 1: Synthesis parameters used in numerical simulations

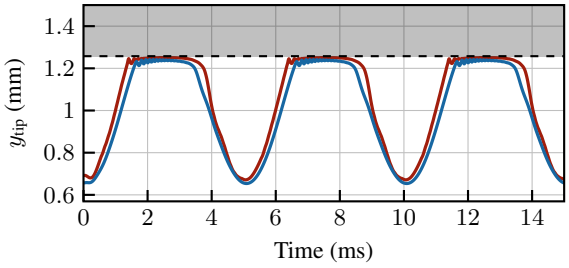

Figure 5: Comparison between the proposed model and the model in [5] under similar experimental condition in said paper.

6.3. Comparison with Avanzini and van Walstijn model

A separate study was conducted to compare the proposed model to the model in [5] in a dynamic simulation without any coupled acoustics. An external 200 Hz sinusoidal driving force with an amplitude range from 0-90 N was applied across the entire reed surface. In an attempt to match the simulations, the following parameters were modified: $k_{\text{lay}} = 3 \times 10^7$ N/m$^\alpha$, $y_{\text{lip}} = 0.5$ mm. A much lower lay stiffness was necessary because the ad hoc collisions in [5] result in a much weaker interaction between the reed and lay. Fig. 5 demonstrates that the proposed model can be modified to produce similar responses to the model in [5].

6.4. Lip parameter experiments

Fig. 6 displays two preliminary experiments where, in the top plot, the lip position is linearly increased over 0.5 s by 6 mm and 1 mm in the x and y directions, respectively. In the bottom plot, the lip stiffness is linearly increased over 0.5 s to 1×10^7 N/m$^\alpha$. The result in both is a pitch shift up most clearly evident in the energy of the higher partials. However, the timbre of the two variations are markedly different.

7. CONCLUSION

A model for the single-reed has been presented that decouples the material parameters of the reed from the player. An efficient numerical scheme was developed by representing the reed using an approximate modal expansion and modeling collisions using the SAV approach. The approximate modal expansion approach was demonstrated to have accuracy on par with the linearly implicit θ-scheme utilizing 512 grid points. The proposed scheme is linearly implicit and requires a linear system inverse at each time step. The proposed reed model is coupled to an optimized modal response fitted to the input impedance of an alto saxophone.

Viscoelastic collision with two distributed barriers were modeled by using one auxiliary variable, two gradient vectors, and fixing the nonlinear damping parameters to their nominal values. Non-negativity of the auxiliary variable is ensured by scaling one of the gradient vectors. Further investigation is needed into robustness of this approach. A particular concern is the assumption that the acoustic force can be ignored in the auxiliary variable constraint. Although no anomalous behavior has been observed so far,

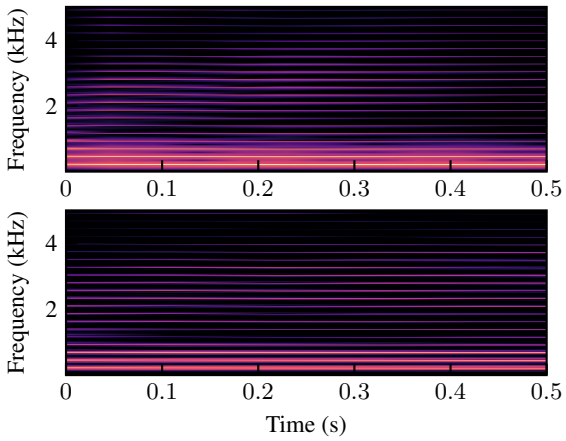

Figure 6: Synthesis experiments with different lip parameters. Top: increasing x_{lip} and y_{lip} by 6 mm and 1 mm. Bottom: increasing the lip stiffness to 1×10^7 N/m$^{\alpha}$

a stronger constraint would consider the contribution of the acoustic force.

A benefit of separating player parameters and reed parameters is that control of the synthesis algorithm is more physically informed. The tuning and register of each note can be adjusted through the same movements an actual player would make, such as adjusting their lip position or tightening their embouchure. Another benefit is that the material parameters of the reed and mouthpiece can be directly inferred from physical measurements. The model also allows for great flexibility and better control of playing parameters. Though not explored here, it is possible to spatially vary the stiffness and damping along each barrier. There remains, for future work, the classical issue of determining a parameter space suitable for sound synthesis.

8. ACKNOWLEDGMENTS

CD would like to thank Maarten van Walstijn for advice regarding implicit schemes and damping in the HC model.

9. REFERENCES

[1] A. Chaigne and J. Kergomard, *Acoustics of Musical Instruments*, Springer-Verlag, New York, NY, 2016.

[2] J. Backus, "Small-vibration theory of the clarinet," *J. Acoust. Soc. Am.*, vol. 35, pp. 305–313, 1963.

[3] M. van Walstijn and F. Avanzini, "Modelling the mechanical response of the reed-mouthpiece-lip system of a clarinet. part II: a lumped model approximation," *Acta Acust. united Acust.*, vol. 93, pp. 435–446, 2007.

[4] V. Chatziioannou, S. Schmutzhard, and S. Bilbao, "On iterative solutions for numerical collision models," in *Proc. 20th Int. Conf. Digital Audio Effects (DAFx-17)*, Edinburgh, UK, 2017, pp. 72 – 79.

[5] F. Avanzini and M. van Walstijn, "Modeling the mechanical response of the reed-mouthpiece-lip system of a clarinet. part I. a one-dimensional distributed model," *Acta Acust. united Acust.*, vol. 90, pp. 537–547, 2004.

[6] Y.-C. Fung, *Biomechanics: mechanical properties of living tissue*, Springer Science + Business Media, New York, USA, 1993.

[7] M. Ducceschi and S. Bilbao, ," in *Proc. 22nd Conf. Digital Audio Effects (DAFx-19)*, Birmingham, UK, 2019.

[8] M. van Walstijn, V. Chatziioannou, and A. Bhanuprakash, "Implicit and explicit schemes for energy-stable simulation of string vibrations with collisions: Refinement, analysis, and comparison," *J. Sound Vib.*, vol. 569, pp. 117968, 2024.

[9] S. Bilbao, R. Russo, C. J. Webb, and M. Ducceschi, "Real-time guitar synthesis," in *Proc. of the 27th Int. Conf. Digital Audio Effects (DAFx24)*, 2024, pp. 163–170.

[10] L. Meirovitch, *Fundamentals of vibrations*, McGraw-Hill, Boston, MA, 2001.

[11] M. Ducceschi, *Nonlinear Vibrations of Thin Rectangular Plates: A Numerical Investigation with Application to Wave Turbulence and Sound Synthesis*, Ph.D. thesis, ENSTA ParisTech, 2014.

[12] K. Hunt and F. Crossley, "Coefficient of restitution interpreted as damping in vibroimpact," *J. Appl. Mech.*, vol. 42, no. 2, pp. 440–445, 1975.

[13] V. Chatziioannou, S. Schmutzhard, M. Pàmies-Vilà, and A. Hofmann, "Investigating clarinet articulation using a physical model and an artificial blowing machine," *Acta Acust. united Acust.*, vol. 105, pp. 682–694, 11 2019.

[14] J. Sun, N. Lam, L. Zhang, D. Ruan, and E. Gad, "A note on Hunt and Crossley model with generalized visco-elastic damping," *Int. J. Impact Eng.*, vol. 121, pp. 151–156, 2018.

[15] M. van Walstijn, V. Chatziioannou, and N. Athanasopoulos, "An explicit scheme for energy-stable simulation of mass-barrier collisions with contact damping and dry friction," in *Proc. 8th IFAC Workshop on Lagrangian and Hamiltonian Methods for Nonlinear Control (LHMNC 2024)*, 2024, pp. 214–219.

[16] J. Shen, J. Xu, and J. Yang, "The scalar axuiliary variable (SAV) approach for gradient flows," *J. Comput. Phys.*, vol. 353, pp. 407–416, 2018.

[17] S. Bilbao, M. Ducceschi, and F. Zama, "Explicit exactly energy-conserving methods for hamiltonian systems," *J. Comp. Phys.*, vol. 472, pp. 111697, 2023.

[18] C. C. Darabundit and G. Scavone, "Discrete port-Hamiltonian system model of a single-reed woodwind instrument," *Front. Signal Process.*, vol. 5, 2025.

[19] E. Maestre, G. Scavone, and J. O. Smith, "Joint modeling of impedance and radiation as a recursive parallel filter structure for efficient synthesis of wind instrument sounds," in *Proc. 21st Int. Conf. Digital Audio Effects (DAFx-18)*, Averiro, Portugal, 2018, pp. 157–164.

[20] M. van Walstijn and J. Bridges, "Simulation of distributed contact in string instruments: a modal expansion approach," in *Proc. 24th Eur. Signal Process. Conf. (EUSIPCO-2016)*, Budapest, Hungary, 2016, pp. 1023–1027.

[21] R. Russo, M. Ducceschi, and S. Bilbao, "Efficient simulation of the bowed string in modal form," in *Proc. 25th Int. Conf. Digital Audio Effects (DAFx20in22)*, Vienna, Austria, 2022, pp. 122–129.

[22] W. L. Li, "Free vibrations of beams with general boundary conditions," *J. Sound Vib.*, vol. 237, no. 4, pp. 709–725, 2000.

[23] S.-H. Jang and J.-G. Ih, "On the multiple microphone method for measuring in-duct acoustic properties in the presence of mean flow," *J. Acoust. Soc. Am.*, vol. 103, pp. 1520–1526, 1998.

[24] G. P. Scavone, "An open-source project for wind instrument modeling using digital waveguides," in *186th Meet. Acoust. Soc. Am.*, 2024.

[25] E. Maestre, J. S. Abel, J. O. Smith, and G. P. Scavone, "Constrained pole optimization for modal reverberation," in *Proc. 20th Int. Conf. Digital Audio Effects (DAFx-17)*, Edinburgh, UK, 2017, pp. 381–388.

[26] N. I. M. Gould, S. Lucidi, M. Roma, and P. L. Toint, "Solving the trust-region subproblem using the lanczos method," *SIAM Journal on Optimization*, vol. 9, no. 2, pp. 504–525, 1999.